Global near real-time flood mapping using a fully automated Sentinel-1-based processing chain

Christian Böhnke[1]✉, Sandro Martinis[1], Michael Nolde[1], Stefan Schlaffer[2], Torsten Riedlinger[1]

[1] Deutsches Zentrum für Luft- und Raumfahrt (DLR), Germany;
[2] Department of Geodesy and Geoinformation, Vienna University of Technology
✉ christian.boehnke@dlr.de

Keywords: flood, SAR, flood mapping, processing chain

1. Introduction

Fast-growing population numbers and climate change as a driving force for extreme meteorological events lead to an increasing impact of natural disasters on the environment in general and human life in particular. Concurrently, technical developments strongly enable a better spacecraft-driven earth observation resulting in an increasing demand for rapid crisis mapping products (Voigt, et al., 2016).

Of all globally monitored natural disasters floods occurred with a frequency of 39 % in the period from 1980 to 2015 (Munich RE, 2016). This number emphasizes the need for a global time-independent flood monitoring followed by information about the spatial distribution of flooded areas. This information directly serves as an input for end users, e.g. rescue forces in the field, insurance companies, planners of infrastructure, etc.

In this article, we demonstrate an automated processing chain automatically deriving flood information from globally acquired Sentinel-1 data. We first describe the data used and further elaborate on the methodology in more detail. The processing chain has been designed to compute global data and currently operates on different areas of interest all over the world. However, we apply the methodology to a single-use case in Kerala, India, and discuss the benefits and disadvantages of a radar-based flood detection system. We conclude this article with the further use of the results in the form of a web-based presentation as well as crisis mapping products.

2. Data

The processing chain derives flood information from Sentinel-1 data. Due to its physical properties, Sentinel-1 as a radar satellite operates independently from cloud cover or illumination. This makes it an ideal tool for full-time flood observation during extreme meteorological events which are usually accompanied by a dense cloud cover and therefore often limit optical remote sensing methods.

Sentinel-1 describes a pair of two satellites Sentinel-1A and Sentinel-1B, orbiting the earth in the same orbital plane 180° apart. Both satellites carry a C-band SAR instrument. Each satellite has a repeat cycle of 12 days (Supplementary Fig. 1). The acquisition frequency highly depends on the region. As a European satellite mission within the Copernicus program, the acquisition frequency for mainland Europe is 6 days.

By default, Sentinel-1 acquires data in VV polarization mode (vertical emit and vertical receive). The polarization mode VH (vertical emit and horizontal receive) is widely available but not always provided (Supplementary Fig. 2).

3. Methodology

We use an automated processing chain written in the high-level programming language Python to compute the flood extent from radar data. The processing chain was originally developed for TerraSAR-X data (Martinis, Twele and Voigt, 2009; Martinis, Kersten and Twele, 2015) and has been extended to also include Sentinel-1 data (Twele, et al., 2016). The workflow is depicted in Fig. 1 and describes the major steps from retrieving the raw data through the main processing procedure where water masks are generated. This happens by computing a threshold, separating the radar image into the thematic classes water and non-water. By targeting two thematic classes as output we require a bimodal backscatter distribution. Therefore, we do not compute the threshold on the entire radar image but on selected image tiles fulfilling the requirement of a bimodal distribution. In a final step, we integrate a fuzzy logic approach to refine the classification result. This step is followed by a region growing implementation to include or exclude further locations not covered by the last steps. The final product is a binary water mask with the information if a pixel holds water or non-water. We distribute the results through an in-house web client to be available for researchers and project partners.

3.1. Data Ingestion

We use ground range detected (GRD) Sentinel-1 data in the VV polarization, acquired in the interferometric wide swath mode (IW). The use of VV polarization is preferred over VH, as dual-

Proceedings of the 5th International YES Congress
DOI: 10.2312/yes19.01

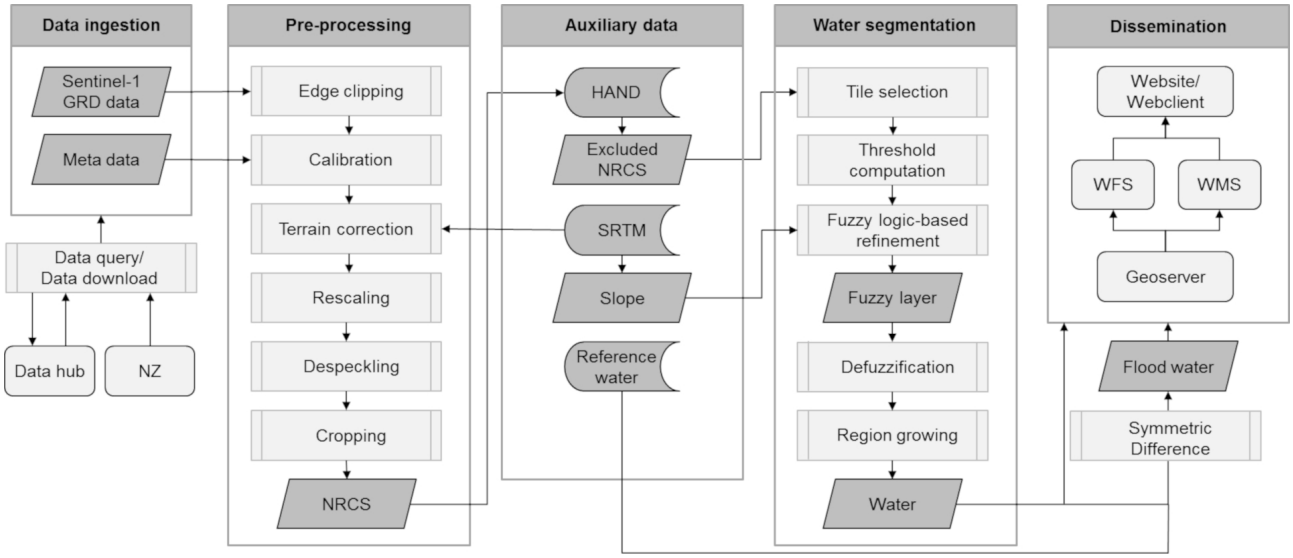

Figure 1: Workflow of the automated Sentinel-1 processing chain.

polarized data dominantly accounts for volume scattering, e.g. over tree canopies. This scattering mechanism is currently not investigated and would add a substantial processing load.

Data is retrieved either through constantly requesting new data from the Sentinel-1 Data Hub of the European Space Agency (ESA) or through data ingestion directly from one of the facilities of the German Aerospace Center (DLR) in Neustrelitz, receiving data directly via an antenna. The entire processing chain is event-driven, i.e. the computation starts as soon as new data is available.

3.2. Pre-processing

Pre-processing requires a radiometric calibration to sigma naught, thus, converting the digital numbers of the input image to physical units, decibels (dB). In a second step, we apply a Range-Doppler terrain correction on the basis of data from the Shuttle Radar Topography Mission (SRTM). All of these steps are performed through the software *snappy*, a Python wrapper around ESA's Sentinel Application Platform SNAP (ESA 2020). The image output of this step is the normalized radar cross section (NRCS) giving information about the radar backscatter in dB for each image pixel.

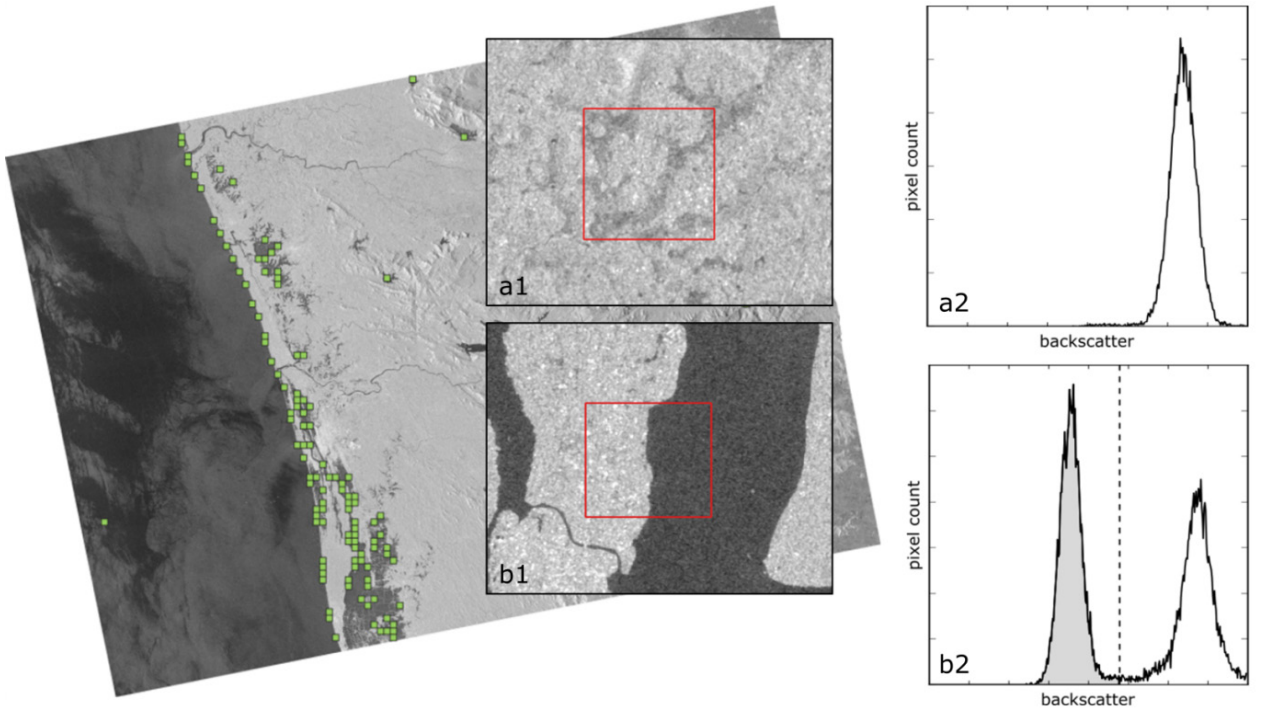

Figure 2: Selected tiles (green) have a low mean backscatter value and a high standard deviation of children mean backscatter values. Two subsets show the effect of these conditions. Subset a1 has a high mean backscatter value and a unimodal backscatter distribution a2, not allowing to separate the histogram into two classes. In contrast to that, subset b1 has a low mean backscatter value and also shows two distinct brightness regimes as can also be seen in the bimodal backscatter distribution b2. Therefore, subset b1 serves as a suitable candidate for threshold computation. The separating threshold is marked with a dashed line.

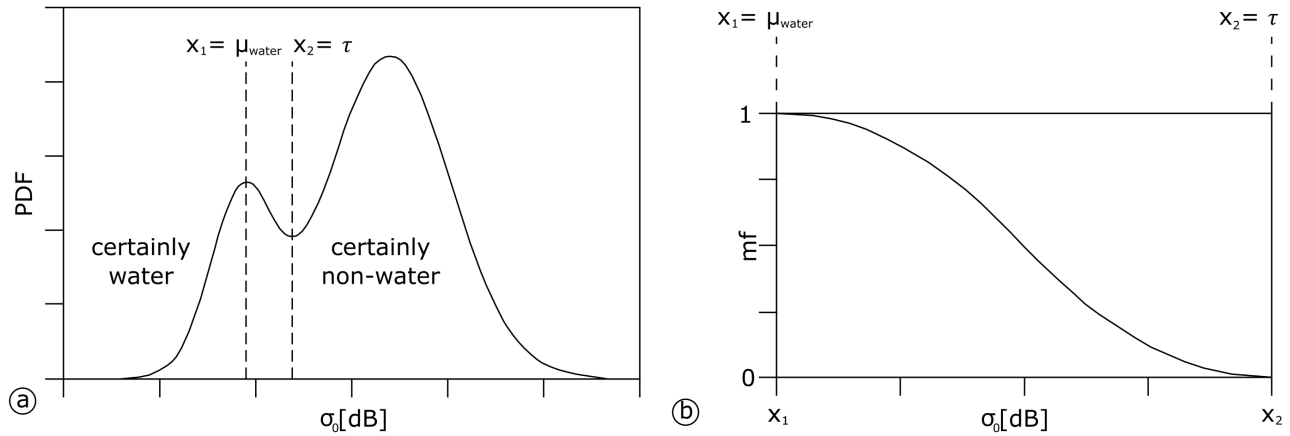

Figure 3: (a) The threshold τ is computed from the backscatter distribution and marks the class break between water and non-water. When applying the threshold to the entire scene μ_{water} describes the mean backscatter value in the water regime. (b) The mean of all water pixels μ_{water} describes locations with a high classification certainty whereas the threshold τ describes locations with a low classification certainty. This is due to the fact that pixel values close to τ may also be misclassified as the underlying backscatter value is caused both by the presence of water and non-water.

3.3. Tiling

After finishing the pre-processing step, the resulting NRCS serves as an input dataset for the following thematic processing task. However, not all areas in the NRCS are suitable for water processing. Nobre, et al. (2011) produced the HAND layer (height above the nearest drainage) to exclude any location with a certain vertical distance from the next drainage. These areas are mainly subject to direct runoff and unlikely to hold enough water for a long period of time. Thus, these areas are to be excluded from the calculation.

In a further step, we divide the NRCS image into quadratic non-overlapping parent tiles and only keep tiles with more than 50 % valid pixels where non-valid pixels are a byproduct of the HAND based exclusion. We then sub-divide each remaining parent tile into 4 quadratic non-overlapping child tiles and record the mean pixel value for each of the sub-tiles. Only tiles with a low mean backscatter value on the parent level as well as a high standard deviation of all means on child-level are suitable for threshold computation (Fig. 2). Requiring a low mean backscatter value corresponds with the physical property of radar data where smooth surfaces like water result in a low backscatter value. Requiring a high standard deviation of the children means ensures to have a bimodal backscatter distribution and thus, a higher probability of having both water and non-water in one tile.

3.4. Thresholding & fuzzy logic

Martinis, et al. (2009) have discussed major image segmentation techniques to extract water information from radar backscatter. In Twele, et al. (2016) they concluded that the algorithm of Kittler and Illingworth (1986) gives the best results. The algorithm computes a cost function and separates the radar backscatter information for each tile into two distinct classes, i.e. water and non-water in the case of our application. The goal is to decrease the effort to separate these classes on the basis of the histogram of the backscatter values. Thus, the separation optimum marks a threshold τ in the unit of the specific pixel value (Fig. 3a).

The threshold is applied to the entire scene and splits the radar image into the two thematic classes. However, the class break is naturally rather imprecise. We, therefore, use a fuzzy logic approach to analyze the membership of any pixel between the computed threshold τ and the mean value of all water pixels μ_{water} (Fig. 3b).

Pixels with a value close to μ_{water} are assigned with a high degree of membership to the class water as they plot well in the class' regime. Pixel values with a greater distance to μ_{water} towards the threshold τ share a higher uncertainty of being classified correctly and are therefore assigned with a low degree of membership to the class water, respectively with a high degree of membership to the class non-water.

Based on that information the first classification result is refined to exclude certain locations with a weak membership to the class water.

The final image is a binary water mask and will be presented in the next section.

4. Use case

In August 2018 the south-Indian state Kerala was affected by unusual monsoon rainfall resulting in the severest flood in decades. The Government of India (2018) reported a deviation in precipitation of 164 % for August 2018 and stated the entire state of Kerala to be affected. The event triggered the International Charter "Space and Major Disasters" for immediate

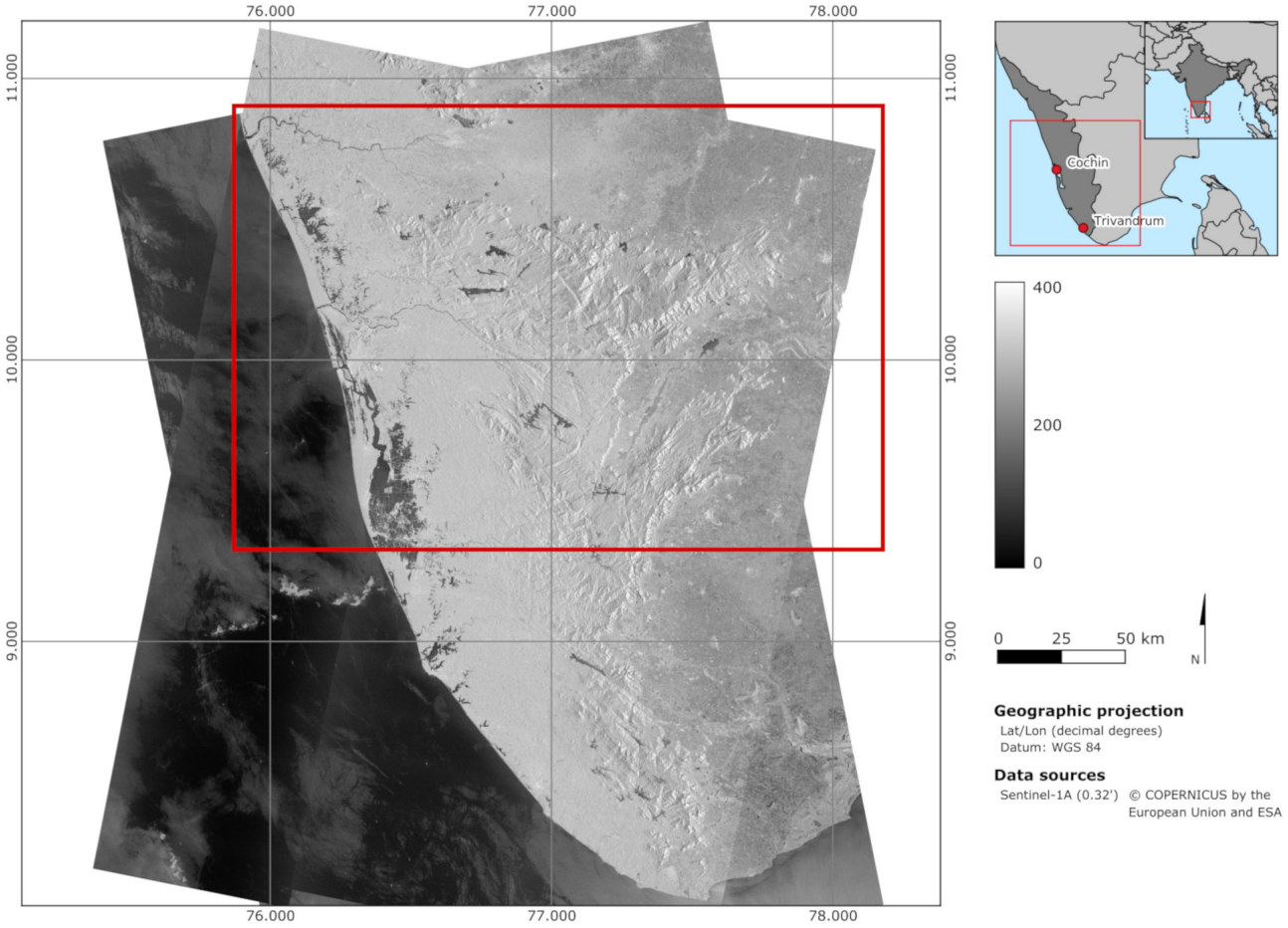

Figure 4: Overview of the study area. Background: 4 Sentinel-1A scenes from descending and ascending path (2 each), acquired on 21 August 2018, VV polarization (© Copernicus data/ESA 2018).

crisis information on the basis of satellite imagery. We took advantage of this situation to check the accuracy of the processing chain and promote further thematic development.

Due to the event, the ESA tasked Sentinel-1 not only to record on the descending path but to also acquire data on the ascending path. We present the output of our processing chain based on the initial

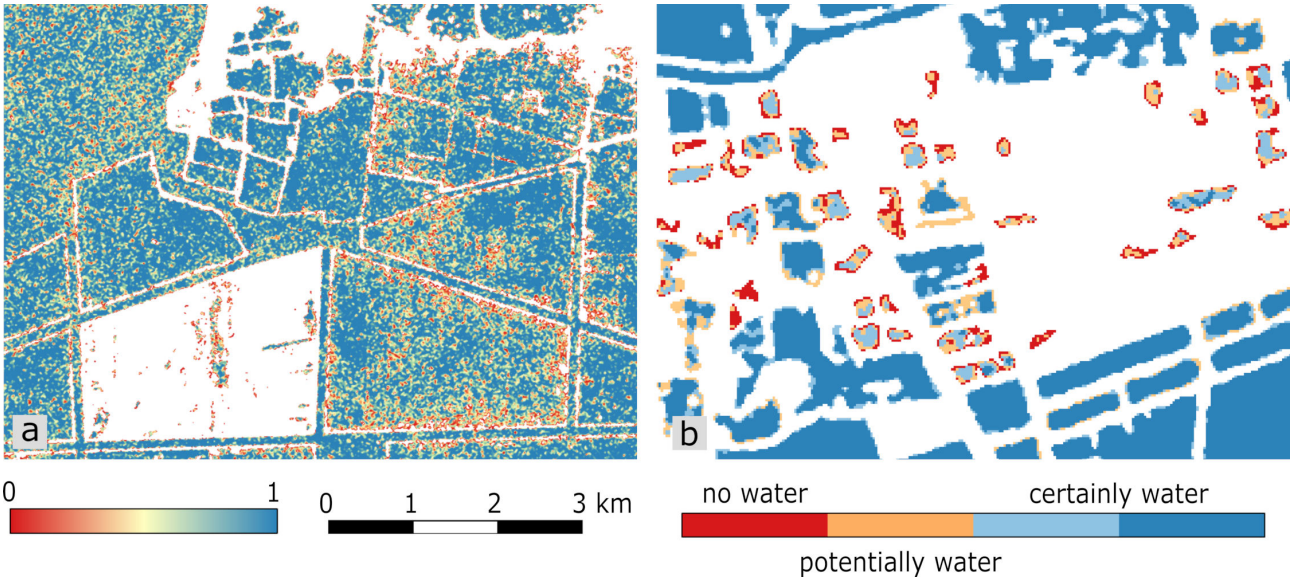

Figure 5: (a) Fuzzy logic-based refinement of NRCS values. Locations with a higher backscatter value are assigned with a low membership degree and thus, a low fuzzy value (close to 0). Locations with lower backscatter are assigned with a high fuzzy value (close to 1). Low fuzzy values mostly plot along edges and are likely to be water-lookalikes. Lower and medium fuzzy values in the center of potentially water patches are usually caused by rough water surfaces, e.g. from wind-induced waves resulting in higher backscatter values. (b) Categorical result of the fuzzy logic-based refinement. Locations with a certain fuzzy value are likely to be water whereas locations with very low fuzzy values are unlikely to be water. Those areas are to be excluded. Locations with medium fuzzy values are subject to region growing and may be re-included.

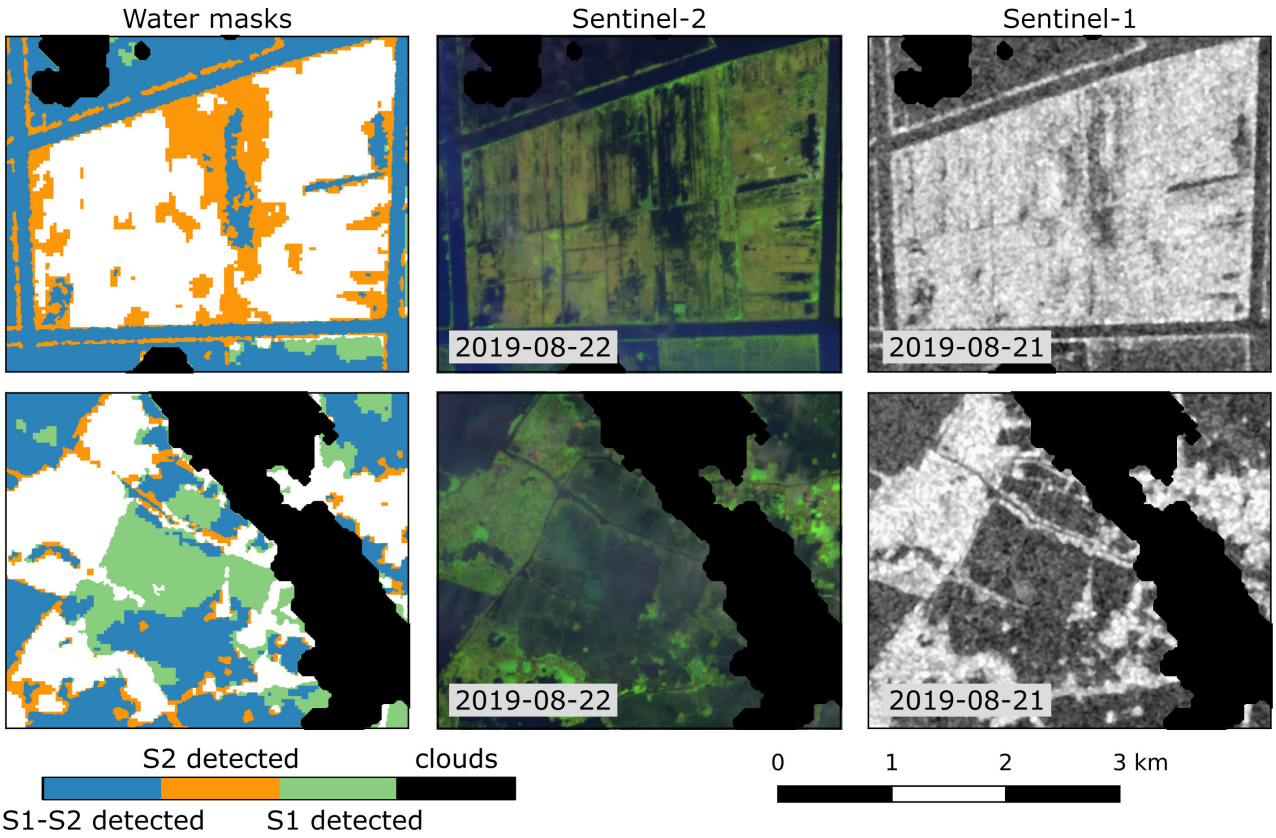

Figure 6: (left) water either detected by Sentinel-1, Sentinel-2, or both. Further subsets show the corresponding Sentinel-2 patch (middle) and Sentinel-1 patch (right). The upper row clearly shows the limitation of radar systems being sensitive to higher surface roughness resulting in non-detected water areas. In contrast to that, the lower row shows the limitation of optical systems where areas are not specifically cloud-covered (see black cloud mask). However, the occurrence of very fine clouds in the center of the path results in a significant change of the spectral signature and thus non-detected water areas.

data and focus on a Sentinel-1 scene in the northern part of the study area (Fig. 4).

Based on the tiling procedure and the thresholding algorithm we get information about water locations. Through the fuzzy logic-based refinement we further exclude location with low certainties of being water (Fig. 5).

5. Discussion

Like every derived dataset, the resulting water masks are not without errors and are highly dependent on the in-situ situation.

The following conditions are likely to cause misclassifications: wind-induced waves roughening the surface and non-water objects with similar backscatter patterns like water, e.g. sand surfaces.

Fig. 5a shows that water bodies are slightly disturbed rather than perfectly smooth, whereas the latter is the ideal behavior.

Wind-induced waves are a common source for misclassifications, especially during extreme meteorological events which are also responsible for floodings. As water surfaces are usually smooth compared to the surrounding area, an increase in surface roughness has a significant impact on the final threshold value. Rough areas within water bodies actually being water by ground truth can have a low fuzzy value, thus, a decreasing certainty for a correct classification.

Water-lookalikes such as sandy features and dunes tend to have similar surface geometries compared to water. Thus, the signal return of water and sand features is nearly the same, challenging the distinction of these classes. Problems arise when observing water objects adjacent to sandy features. In this case, the transition is rather fuzzy and both features may not be differentiated properly. It is also not unlikely to misidentify sand features as water since their fuzzy logic values tend to be similar.

These points underline the fact, that the use of fuzzy logic as an intermediate step helps to refine the initial classification but should not be used solely as a tool for error classification.

In order to solve these challenges, we developed a second processor analyzing Sentinel-2 optical data (Wieland, 2019a; Wieland, 2019b). Sentinel-2, as an optical sensor, has the advantage of being less sensitive to surface disturbances compared to Sentinel-1, as water bodies are detected based on their spectral signature. However, a limitation of the optical system is their sensitivity to cloud cover.

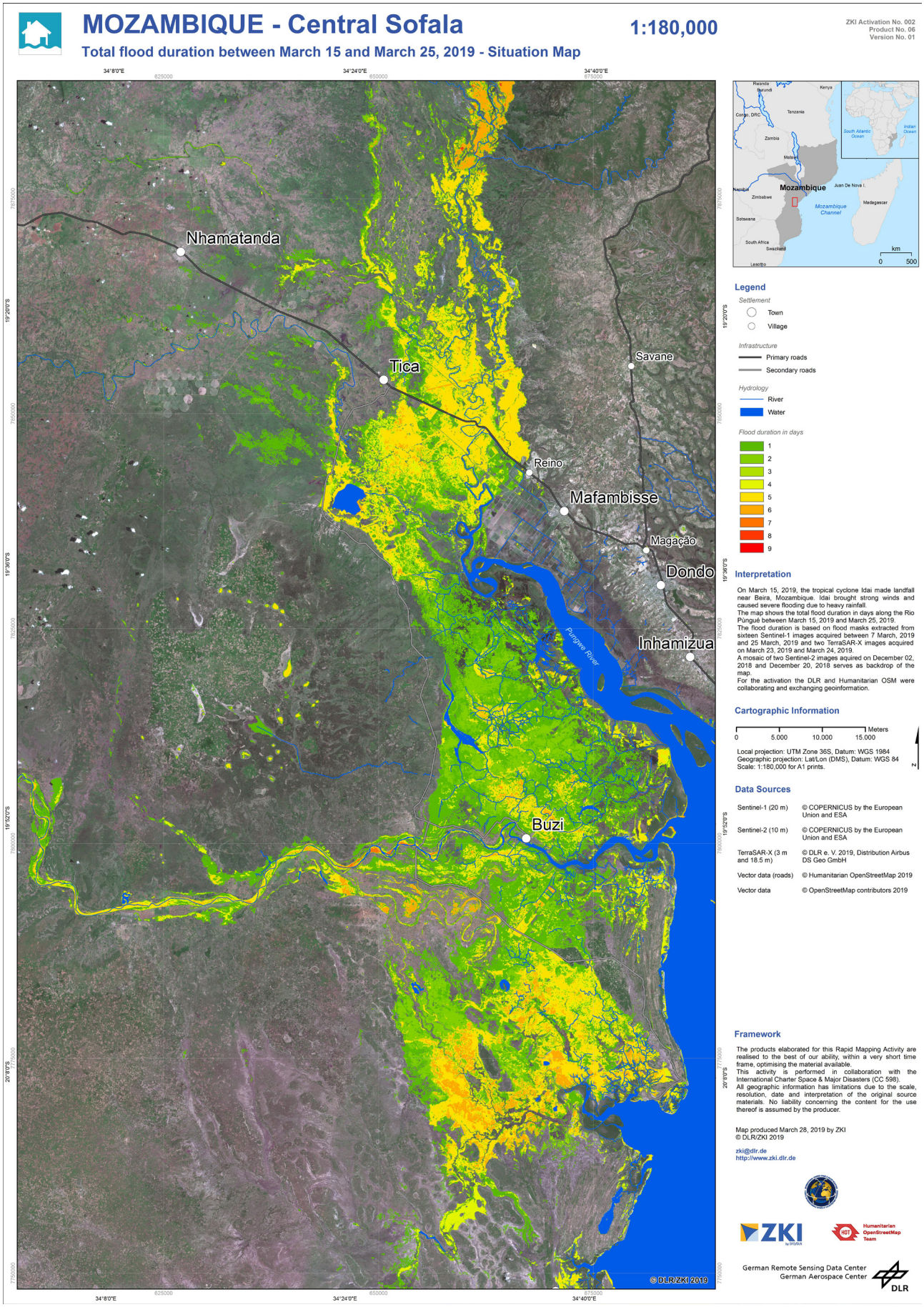

Figure 1: Flood duration map for the area around Buzi, Mozambique. In March 2019 the cyclone Idai made landfall on the east coast of Mozambique resulting in severe floods. Colors of red depict locations with flood duration up to 9 days.

Fig. 6 shows a comparison of Sentinel-1 and Sentinel-2 water masks. Both systems have their benefits and disadvantages, which are highlighted in the subsets.

Further accuracy can be added through the exploitation of VH polarized data, being a frequent effect over tree canopies. By that, flooded vegetation could be detected as well which is to the current state not sufficiently mapped with VV data solely.

6. Conclusions

In connection with extreme meteorological events causing flooding, SAR sensors have proven to give good results. By using an automated system we are able to reduce human interaction and provide a 24/7 data production service. We further distribute the results of the processing through a web client, which is automatically equipped with the latest results whenever available. In the current stage, this web client is not publicly exposed but available to project partners and users of the Center for Satellite Based Crisis Information (ZKI) of the DLR.

A direct use of the results is as input for the computation of flood frequency and flood duration maps (Fig. 7). This information is especially useful for the evaluation of infrastructure as well as which areas were flooded for the longest time and may be sensitive to outbreaks of flood-related diseases.

However, radar sensors have certain physical limitations. Our goal is to enhance the pre-existing processing chain to also include optical data, thus eliminating the disadvantages of both sensor systems.

7. Supplementary material

Supplementary data to this article can be found online at http://doi.org/10.2312/yes19.01.

8. References

Martinis, S., J. Kersten, and A. Twele, 2015. A Fully Automated TerraSAR-X Based Flood Service. ISPRS Journal of Photogrammetry and Remote Sensing 104, 203–212. https://doi.org/10.1016/j.isprsjprs.2014.07.014.

Martinis, S., A. Twele, and S. Voigt, 2009. Towards Operational near Real-Time Flood Detection Using a Split-Based Automatic Thresholding Procedure on High Resolution TerraSAR-X data. Natural Hazards and Earth System Sciences 9, 303–314. https://doi.org/ 10.5194/nhess-9-303-2009.

Government of India, 2018. Study Report: Kerala flood of August 2018. Hydrological Studies Organisation, Central Water Commission, New Delhi, 46 pp. [online] Available at: https://reliefweb.int/report/india/study-report-kerala-floods-august-2018-september-2018 [Accessed 14 August 2020].

Kittler, J. and Illingworth, J. 1986. Minimum error thresholding. Pattern Recognition 19, 41–47. https://doi.org/10.1016/0031-3203(86)90030-0.

Münchener Rückversicherungs-Gesellschaft, 2016. NatCatSERVICE: Loss events worldwide 1980 – 2015, [online] Available at: https://reliefweb.int/report/world/natcatservice-loss-events-worldwide-1980-2015 [Accessed 13 August 2020].

Nobre, A., Cuartas, L., Hodnett, M., Rennó, C., Rodrigues, G., Silveira, A., Waterloo, M. and Saleska, S. 2011. Height Above the Nearest Drainage – a hydrologically relevant new terrain model. Journal of Hydrology 404, 13–29. https://doi.org/10.1016/j.jhydrol.2011.03.051.

European Space Agency, 2020: Sentinel Application Platform, [online] Available at: https://github.com/senbox-org/snap-engine [Accessed 13 August 2020]

Twele, A., Cao, W., Plank, S. and Martinis, S. 2016. Sentinel-1-based flood mapping: a fully automated processing chain. International Journal of Remote Sensing 37, 2990–3004. https://doi.org/10.1080/01431161.2016.1192304.

Voigt, S., Giulio Tonolo, F., Lyons, J., Kucera, J., Jones, B., Schneiderhan, T., Platzeck, G., Kaku, K., Hazarika, M., Czaran, L., Li, S., Pedersen, W., James, G., Proy, C., Macharia, D., Bequignon, J., Guha-Sapir, D., 2016. Global trends in satellite-based emergency mapping. *Science* 353, 247-252. https://doi.org/10.1126/science.aad8728.

Wieland, Marc und Martinis, Sandro (2019a) A modular processing chain for automated flood monitoring from multi-spectral satellite data. Remote Sensing 11, 2330. https://doi.org/10.3390/rs11192330.

Wieland, Marc und Yu, Li und Martinis, Sandro (2019b) Multi-sensor cloud and cloud shadow segmentation with a convolutional neural network. Remote Sensing of Environment 230, 111203. https://doi.org/10.1016/j.rse.2019.05.022.